Received: 28 August 2020 | Accepted: 26 March 2021

DOI: 10.1002/nbm.4527

RESEARCH ARTICLE

NMR IN BIOMEDICINE WILEY

Fast and accurate modeling of transient-state, gradient-spoiled sequences by recurrent neural networks

Hongyan Liu | Oscar van der Heide | Cornelis A. T. van den Berg | Alessandro Sbrizzi

Center for Image Sciences, University Medical Center Utrecht, Utrecht, the Netherlands

Correspondence
Hongyan Liu, University Medical Center, Heidelberglaan 100, 3508 GA, Utrecht, the Netherlands.
Email: h.liu@umcutrecht.nl

Funding information
China Scholarship Council

Fast and accurate modeling of MR signal responses are typically required for various quantitative MRI applications, such as MR fingerprinting. This work uses a new extended phase graph (EPG)-Bloch model for accurate simulation of transient-state, gradient-spoiled MR sequences, and proposes a recurrent neural network (RNN) as a fast surrogate of the EPG-Bloch model for computing large-scale MR signals and derivatives. The computational efficiency of the RNN model is demonstrated by comparisons with other existing models, showing one to three orders of acceleration compared with the latest GPU-accelerated, open-source EPG package. By using numerical and in vivo brain data, two used cases, namely, MRF dictionary generation and optimal experimental design, are also provided. Results show that the RNN surrogate model can be efficiently used for computing large-scale dictionaries of transient-state signals and derivatives within tens of seconds, resulting in several orders of magnitude acceleration with respect to state-of-the-art implementations. The practical application of transient-state quantitative techniques can therefore be substantially facilitated.

KEYWORDS
Bloch equation, extended phase graph, MR fingerprinting, quantitative MRI, recurrent neural networks

1 | INTRODUCTION

Quantitative magnetic resonance imaging (qMRI) aims at reconstructing various magnetic properties of tissues, such as relaxation times and proton density (PD). Such quantitative tissue parameter maps may reveal pathological information about organs that are theoretically independent of MR protocols, and therefore they may lead to a more objective and precise clinical diagnosis.[1,2] Recent qMRI methods, such as MR fingerprinting (MRF)[3] and MR-STAT,[4] usually use relatively short sequences, during which the magnetization is in a transient state, to encode multiple quantitative parameters into the measured signal simultaneously. To perform the quantitative reconstructions, the spin dynamics needs to be simulated according to the physical model of the MR signal, for example, the Bloch equation or the extended phase graph (EPG).[5]

Abbreviations used: AD, automatic differentiation; CRLB, Cramér–Rao lower bound; DE, differential evolution; EPG, extended phase graph; GPU, graphics processing unit; GRU, gated recurrent unit; MAE, mean absolute error; MAPE, mean absolute percentage error; MRF, magnetic resonance fingerprinting; MR-STAT, magnetic resonance spin tomography in time domain; NRMSE, normalized root mean square error; qMRI, quantitative magnetic resonance imaging; RNN, recurrent neural network; SLR, Shinnar–LeRoux; SSFP, steady-state free precession; SVD, singular value decomposition.

Currently, gradient-spoiled, transient-state MR sequences are widely used for qMRI applications,[6–8] because they require relatively short acquisition times, and are not affected by the banding artifacts resulting from the main (B_0) field nonuniformity. For these gradient-spoiled sequences, the EPG formalism is an efficient computational model to simulate the MR signal evolution. Unlike the Bloch equation, which models the temporal MR signal for a single isochromat resonating at a given frequency, the EPG approach models the spins within a voxel as a discrete set of dephasing states, and is an efficient way of simulating spin dephasing induced by unbalanced spoiling gradients.

For various qMRI applications, computing large amounts of MR signals using the EPG models are necessary but also very time-consuming tasks. For example, in MRF methods, a dictionary that contains the temporal signal evolution for different combinations of parameter values (T_1, T_2, B_1^+, etc.) is usually used for reconstructing the pixel-wise properties by a matched filter estimator (dictionary matching).[9] To reconstruct all parameters with high precision, many discretization steps are required for each parameter to be estimated, resulting in a large dictionary that may need a prohibitively long time. Currently, the time required for dictionary generation varies from hours to days, depending on the number of reconstruction parameters included, the physical model used for simulation and the computing hardware. For example, Serrao et al.[10] reported that generating an MRF dictionary with 324 different T_1 values and 537 different T_2 values takes about 0.75 h on 48 parallel central processing units (CPUs). Körzdörfer et al.[11] reported that generating a dictionary including four reconstruction parameters (T_1, T_2, B_0 and B_1^+) takes about 1 week on a fast computer. Furthermore, modification of the sequence acquisition parameters asks for new dictionary computations.

Recently, progress in accelerating MR signal simulations has been made, mainly in two different directions. On one hand, algorithms for large-scale MR signal simulations, based on the exact MR physics models, have been implemented and executed in parallel on graphics processing units (GPUs), and achieve a reasonable acceleration rate.[12,13] On a parallel track, based on recent developments in the field of deep learning, several types of neural networks (NNs), such as generative adversarial networks[14] and fully connected NNs,[15] have been trained as surrogate models to compute MR signals at very high speed. However, one common problem for these NN methods is that they all are currently trained and validated for a fixed MR sequence and only allow limited (if any) sequence parameter inputs such as TE and TR. Therefore, these models have very little flexibility and have to be retrained when a new or slightly modified sequence is applied. Compared with existing network architectures,[14,15] recurrent neural networks (RNNs) are the most widely used deep learning models for time series predictions. Since the RNN models demonstrate the possibility of processing sequence inputs of any length, use shared weights across time, and can be run on both CPUs[16] and GPUs[17,18] efficiently with existing publicly available software implementations, they are highly suitable for accelerating the computation of large-scale MR signal evolution.

Besides simulating temporal MR signals, qMRI applications sometimes also require computing the MR signal derivatives with respect to the reconstruction parameters. For example, derivative computations are usually required for gradient-based optimization algorithms to solve model-based qMRI problems.[4,19] One other example requiring derivative computations is the Cramér–Rao-based optimal experimental design framework for qMRI sequences.[20,21] Signal derivatives can be computed using either the finite difference (FD) or automatic differentiation (AD) method,[20–22] which may at least double the amount of calculation compared with computing only the signal without derivatives.

In this work, we focus on how to accurately and efficiently model MR signal responses for gradient-spoiled sequences. Firstly, a more accurate EPG model, namely EPG-Bloch, is proposed. Currently, widely used EPG models either consider the radiofrequency (RF) pulses as instantaneous spin rotations[6] or correct for the RF slice profile imperfections using an approach that is based on small tip-angle (STA) approximation.[23–26] To better model the imperfect slice profile effects, especially for large flip angles (>60 degrees), the new EPG-Bloch model considers the RF pulse shape and models the RF excitation effects by temporal discretization and substep evolution, analogously to Bloch-based simulation of RF excitation pulses.[27,28]

The EPG-Bloch model proposed here is more accurate, yet computationally more expensive than the standard EPG because it requires simulating both the signal for many dephasing states and the discretization of RF pulses. The long computational time of the EPG-Bloch motivates the use of a fast surrogate model. In this paper, an RNN model with multiple stacked layers[29–31] is applied as a surrogate model for EPG-Bloch. The RNN model takes both tissue parameters and sequence parameters as inputs, and outputs the MR signals as well as their derivatives sequentially. The sequence parameters could be time-varying, such as a transient-state flip-angle scheme.[6–8]

We demonstrate that the RNN model can be trained and used as a fast and accurate surrogate model for EPG-Bloch with an appropriate training dataset, and that it can be conveniently used for large-scale MR signal simulations for different acquisition parameters without any need for retraining. Overall, we show that the RNN model on a GPU accelerates the signal computation by at least a factor of 10^4 compared with the EPG-Bloch model, and is approximately one to three orders of magnitude faster than the state-of-the-art GPU-accelerated EPG simulation package[12] for different sizes of dataset. By using numerical and in vivo experimental data, we provide examples of applications of RNN for rapid MR signal computations, namely, (i) the generation of MRF dictionaries, and (ii) the optimal sequence design based on the Cramér–Rao lower bound (CRLB). In both scenarios, construction of a three-dimensional dictionary and optimization of a 3-s long sequence, the total computation times are within a few seconds.

2 | THEORY

2.1 | EPG-Bloch

The EPG represents the MR signal obtained from a voxel of volume V under the effect of dephasing terms using the Fourier formalism[5]:

$$\begin{aligned}
\tilde{F}_+(\mathbf{k}) &= \int_V (M_x(\mathbf{r}) + iM_y(\mathbf{r}))e^{-i\mathbf{kr}}d\mathbf{r} = \int_V M_+(\mathbf{r})e^{-i\mathbf{kr}}d\mathbf{r},\\
\tilde{F}_-(\mathbf{k}) &= \int_V (M_x(\mathbf{r}) - iM_y(\mathbf{r}))e^{-i\mathbf{kr}}d\mathbf{r} = \int_V M_-(\mathbf{r})e^{-i\mathbf{kr}}d\mathbf{r},\\
\tilde{Z}(\mathbf{k}) &= \int_V M_z(\mathbf{r})e^{-i\mathbf{kr}}d\mathbf{r},
\end{aligned} \tag{1}$$

where $\mathbf{k}$ is the dephasing coordinate for the "configuration state" $\tilde{\mathbf{F}}(\mathbf{k}) = \left[\tilde{F}_+(\mathbf{k}), \tilde{F}_-(\mathbf{k}), \tilde{Z}(\mathbf{k})\right]^T$. For gradient-spoiled sequences, the dephasing term mainly comes from spoiler gradients.

In Weigel,[5] it is shown that the evolution of configuration states for a given MR sequence can be computed by applying different physical operators, such as RF excitation, relaxation and dephasing. To allow for more accurate computations, slice profile correction can be included by discretizing the slice-selective dimension z into N_z subslices, and computing the evolution of these spatially dependent configuration states, $\tilde{\mathbf{F}}(\mathbf{k},z)$, separately.[23,25] The slice profile can be computed by STA approximation,[32] and then multiplied with the original flip angle to obtain the effective flip angles at different slice-selective locations. Note that the rotation effect of the refocusing gradient should also be included in the slice profile computation, especially when the spin rephasing is not perfect, and the computed slice profile will be complex-valued. After computing the EPG signal evolution at all different z locations, the transverse magnetization of the whole slice can be computed by summing up all zero-state signals $\tilde{F}_+(\mathbf{0},z)$.

The slice-profile computation by STA approximation is described by Equation 2,[32]

$$SS(z) = M_{xy}^{RF}(z) = i\gamma M_0 \int_0^{T_{RF}} \bar{B}_{xy}(t)e^{-i\gamma z \int_t^{RF} G_z(s)ds}dt, \tag{2}$$

where T_{RF} is the duration time of the RF pulse, $G_z(t)$ is the amplitude of the linear gradient assuming that z is the slice-selective direction, and $\bar{B}_{xy}(t)$ is the amplitude of the RF excitation pulse, which is normalized to satisfy $i\gamma M_0 \int_0^{T_{RF}} \bar{B}_{xy}(t)dt = 1$. The effective flip angle including slice-profile correction at location z then scales approximately linearly with the transmit RF field heterogeneity B_1^+, the slice profile $SS(z)$ and the amplitude of the RF pulse. The action of the RF pulse with a given effective flip angle in the EPG model can be computed by using eqs 10–12 in Weigel.[5]

Sources of error for standard EPG approximations could be caused by the following combined arguments. Firstly, one of the approximations involved in standard EPG is the fact that for SSFP trains, RF excitations are performed as instantaneous rotations. These effective instantaneous RF rotation angles are calculated either from STA approximation, as explained above[23,25]) or by Shinnar–LeRoux (SLR)[33] methods, both of which are approximation methods. Secondly, in SSFP sequences, the magnetization is repeatedly excited and thus what happens at a given excitation moment has an effect on the subsequent time steps. Consequently, effects from approximations in the RF excitation step cumulatively add up. Finally, the STA and SLR approximations are derived for initial conditions equal to equilibrium. Even if in some cases this could be a good assumption (spoiling sequences "eliminate" transverse components), this is nonetheless an approximation. Consequently, the errors discussed above for single RF excitations can propagate and accumulate during successive RF simulations over the whole SSFP transient-state sequences.

A more accurate method to compute the magnetization response to an RF pulse is to discretize the RF pulse duration time T_{RF} into N_{RF} time intervals of length Δt, and numerically solve the Bloch equation for each time step by applying the operator splitting method.[34,35] Eq. 1.58 in van Valenberg[34] gives a first-order approximated solution for discretized time t_{n+1},

$$\begin{bmatrix} M_x(t_{n+1}) \\ M_y(t_{n+1}) \\ M_z(t_{n+1}) \end{bmatrix} = \mathbf{R}_n\mathbf{D} \begin{bmatrix} M_x(t_n) \\ M_y(t_n) \\ M_z(t_n) \end{bmatrix} + (\mathbf{I} - \mathbf{D})\mathbf{M}_0, \tag{3}$$

where $\mathbf{D} = \exp\left(\begin{bmatrix} e^{-\Delta t/T_2} & 0 & 0 \\ 0 & e^{-\Delta t/T_2} & 0 \\ 0 & 0 & e^{-\Delta t/T_1} \end{bmatrix}\right)$ is the relaxation operator, $\mathbf{R}_n = \exp\left(\gamma\Delta t \begin{bmatrix} 0 & G_z(t_n)\cdot z & -B_1^+\cdot B_y(t_n) \\ -G_z(t_n)\cdot z & 0 & B_1^+\cdot B_x(t_n) \\ B_1^+\cdot B_y(t_n) & -B_1^+\cdot B_x(t_n) & 0 \end{bmatrix}\right)$ is the rotation operator, and $\mathbf{M}_0 = [0,0,M_0]^T$ is the magnetization in equilibrium state.

It is shown in the supporting information (Appendix A) that any linear operator used in a Bloch simulator can also be applied in the EPG model.[36] Therefore, Equation 3 for the Bloch equation model can be transformed into the EPG model as below:

$$\tilde{\mathbf{F}}(\mathbf{k},t_{n+1}) = \begin{cases} \mathbf{S}\mathbf{R}_n\mathbf{D}\mathbf{S}^{-1}\tilde{\mathbf{F}}(\mathbf{k},t_n) + \mathbf{S}(\mathbf{I}-\mathbf{D})\mathbf{M}_0, & \text{if } \mathbf{k}=0, \\ \mathbf{S}\mathbf{R}_n\mathbf{D}\mathbf{S}^{-1}\tilde{\mathbf{F}}(\mathbf{k},t_n), & \text{otherwise,} \end{cases} \tag{4}$$

where $\mathbf{S} = \begin{bmatrix} 1 & i & 0 \\ 1 & -i & 0 \\ 0 & 0 & 1 \end{bmatrix}$ is the similarity transformation matrix defined as in Weigel.[5] We call the EPG model that computes the discretized RF excitation response by Equation 4 EPG-Bloch, since Equation 4 is derived from the approximate Bloch equation solution (Equation 3).

2.1.1 | Computational complexity

The EPG-Bloch model described above is more time-consuming compared with the EPG model with slice profile correction, because it computes the RF pulse response in N_{RF} time steps instead of one instantaneous rotation. When an MR sequence of N_{TR} RF pulses is applied, and N_Z spatial points in the slice-selective direction and N_k configuration states in the EPG model are included, simulating the magnetization signal for one single voxel requires computing Equation 4 for $N_{TR} \times N_Z \times N_k \times N_{RF}$ times. Taking $N_{TR} = 1000, N_Z = 32, N_k = 20$ and $N_{RF} = 100$ as an example, Equation 4 needs to be computed 6.4×10^7 times using the EPG-Bloch model, and the corresponding computation time is about 3.5 s on a Desktop PC using the EPG-Bloch code written in Matlab. Note that even although the new EPG-Bloch model is computationally expensive, simulating gradient-spoiled sequences using the new EPG model is still more efficient compared with multiple isochromat Bloch simulations. Theoretically, to fully simulate a gradient-spoiled sequence, one would need the same number of configuration states N_k in an EPG simulation as the number of isochromats N_{iso}in the Bloch simulation, that is, $N_k = N_{iso} = N_{TR}$.[37] However, in practice, since the configuration states in the EPG model decay through time as a consequence of spin-spin and spin-lattice relaxation, N_k can be substantially lower than N_{TR}, thus the number of configuration states required by the EPG model is much smaller than the number of spatial isochromats required by the Bloch simulator to achieve accurate simulation.[28,37]

2.2 | An RNN as a surrogate model

As a consequence of the increased computational complexity, the EPG-Bloch model requires a potentially prohibitively long computation time. To reduce the time needed to generate a large amount of magnetization signals (e.g. in MRF dictionary generation), an RNN network could be trained as a fast surrogate model to replace the new EPG-Bloch model simulation. RNN models can be effectively used to model time-dependent processes and especially ordinary differential equations (as shown in[29–31]), therefore they are highly suitable for MR signal computations. In contrast to previous work,[14,15] we seek a unique surrogate model that can work for various sequence parameters, such as repetition time, the number of RF excitations (sequence length) and flip-angle trains; therefore, retraining of the network will not be needed when we change the parameters of the sequences. Specifically, an RNN architecture with multiple stacked gated recurrent units (GRUs)[31,38] is selected; the RNN architecture used in this paper is shown in Figure 1. Figure 1A shows the RNN structure for the *n*-th time step, which includes three GRU layers and one linear layer. The inputs for the *n*-th RF pulse include both tissue-specific parameters $\boldsymbol{\theta}$ (e.g. T_1 and T_2) and time-dependent sequence parameters $\boldsymbol{\beta}(n)$, such as $TR(n), TE(n)$ and flip-angle $\alpha(n)$. All of the three GRU layers have the same structure, and they receive hidden state inputs $\boldsymbol{h}_1(n-1), \boldsymbol{h}_2(n-1), \boldsymbol{h}_3(n-1)$ and return the updated $\boldsymbol{h}_1(n), \boldsymbol{h}_2(n), \boldsymbol{h}_3(n)$. The hidden states memorize information based on prior inputs, and can be interpreted as an alternative representation of spin states. The initial hidden states $\boldsymbol{h}_1(0), \boldsymbol{h}_2(0), \boldsymbol{h}_3(0)$ can be computed by adding an initial linear layer $Linear_{init}$, as shown in Figure 1B. The input of the initial linear layer is the initial magnetization vector $\boldsymbol{M}_0$.

The hidden state output of the last GRU layer then passes to another linear layer, generating the output signal $M_{xy}(n)$, which is the transverse magnetization at the *n*-th echo time. Optionally, the linear layer could also directly compute additional derivative signal outputs, $dM_{xy}(n)/d\boldsymbol{\theta}$. Computing derivatives by a linear combination of the RNN outputs does not add computation time, therefore, the proposed solution is a more efficient method compared with FD approximations or AD methods.

The network structure shown in Figure 1A is a one time-step component of the full RNN model. It receives the hidden states from the previous time step, and uses the inputs $\boldsymbol{\theta}$ and $\boldsymbol{\beta}(n)$ at the current time step, and outputs the hidden states and the magnetization signal for the current time step. To complete the full computation of the temporal signal, the one time-step component shown in Figure 1A is recurrently used. That is why this type of network is called an RNN, and explains how the weights are shared in the fully unrolled RNN.

Our RNN implementation of the EPG-Bloch model is available for download at https://gitlab.com/HannaLiu/rnn_epg.

FIGURE 1 Recurrent neural network (RNN) structure for learning the extended phase graph (EPG) model. A, RNN architecture with three stacked gated recurrent units (GRU) for the *n*-th time step. At each time step, GRU1 receives inputs x(n) including tissue parameter θ and time-varying sequence parameter $\beta(n)$. The hidden states $\mathbf{h}_1(n),\mathbf{h}_2(n),\mathbf{h}_3(n)$ are computed and used for the next time step. A linear layer is added after GRU3 to compute the magnetization and derivatives using the hidden state $\mathbf{h}_3(n)$. B, An initial linear layer, *Linear*$_{init}$, is used for computing the initial hidden states $\mathbf{h}_1(0),\mathbf{h}_2(0),\mathbf{h}_3(0)$ from initial magnetization $\mathbf{M}_0$

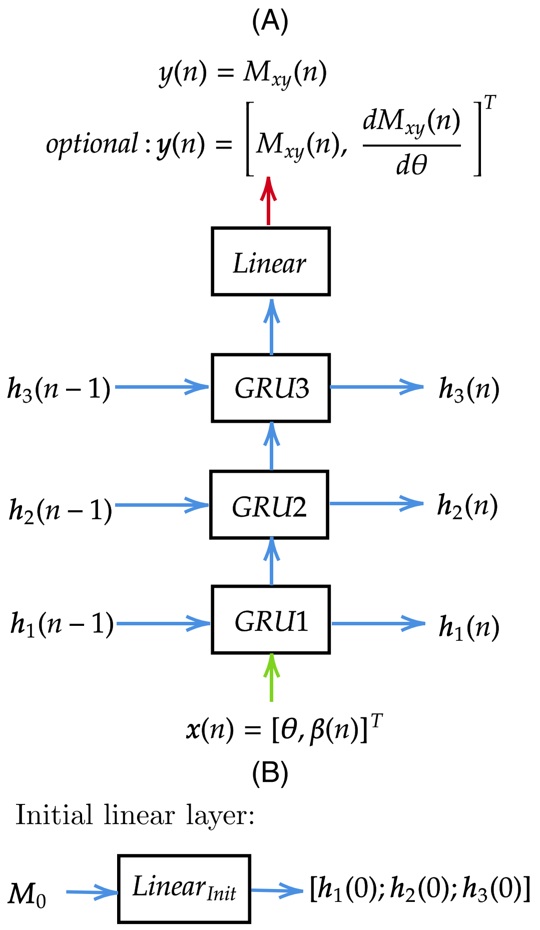

3 | METHODS

3.1 | Validation of the EPG-Bloch model

To demonstrate the accuracy of the newly proposed EPG-Bloch model, experiments were performed on a 1.5-T clinical MR system (Ingenia; Philips Healthcare, Best, the Netherlands). A transient-state, gradient-echo sequence with gradient spoiling and smoothly varying flip-angle train was used. Such transient-state pulse sequences have been used for quantitative MR experiments such as MRF[6] and MR-STAT.[7] A non-selective inversion pulse was applied at the beginning of the sequence to provide better T_1 encoding, and the waveform of the flip-angle train is shown in Figure 2A. A total number of 480 RF pulses was used in the sequence, each of which had a Gaussian-shaped waveform, a transverse slice thickness of 5 mm and a duration of 0.568 ms. The other settings were: inversion time $T_I = 7.74$ ms, repetition time $T_R = 7.38$ ms, and echo time $T_E = 3.73$ ms.

Three gel phantom tubes with different T_1 and T_2 values were imaged separately using the gradient-spoiled sequence described above, with the slice-selective gradient aligned with the longitudinal axes of the tubes. To measure the transverse magnetization signals at each TR, the phase-encoding gradients were switched off; as a consequence, no spatial in-plane encoding was applied, since the material in the tube is homogeneous over the excited transverse slice. Transient state signals for the corresponding sequence were computed by both the conventional EPG model with STA approximation and the newly proposed EPG-Bloch model with RF pulse discretization. For both models, simulations were run for 32 subslices across a distance three times wider than the slice thickness to include the out-of-slice excitation, and 20 EPG configuration states were included. For the EPG-Bloch model, the Gaussian RF pulse was discretized into 16 equally spaced time steps during the simulation. Simulation runtimes for the EPG and EPG-Bloch models were recorded. The measured data were fitted to the dictionary of simulated signals to find the T_1 and T_2 values that gave the best match. Reference T_1 and T_2 values of the tubes were obtained from an interleaved inversion-recovery and multi spin-echo sequence (2DMix) provided by the MR vendor.[39]

The codes for both the conventional EPG and the proposed EPG-Bloch models were implemented in MATLAB based on existing code available online at https://web.stanford.edu/~bah/software/epg/. All EPG model simulations were run on a 3.7-GHz Intel Xeon W-2145 CPU with eight physical cores.

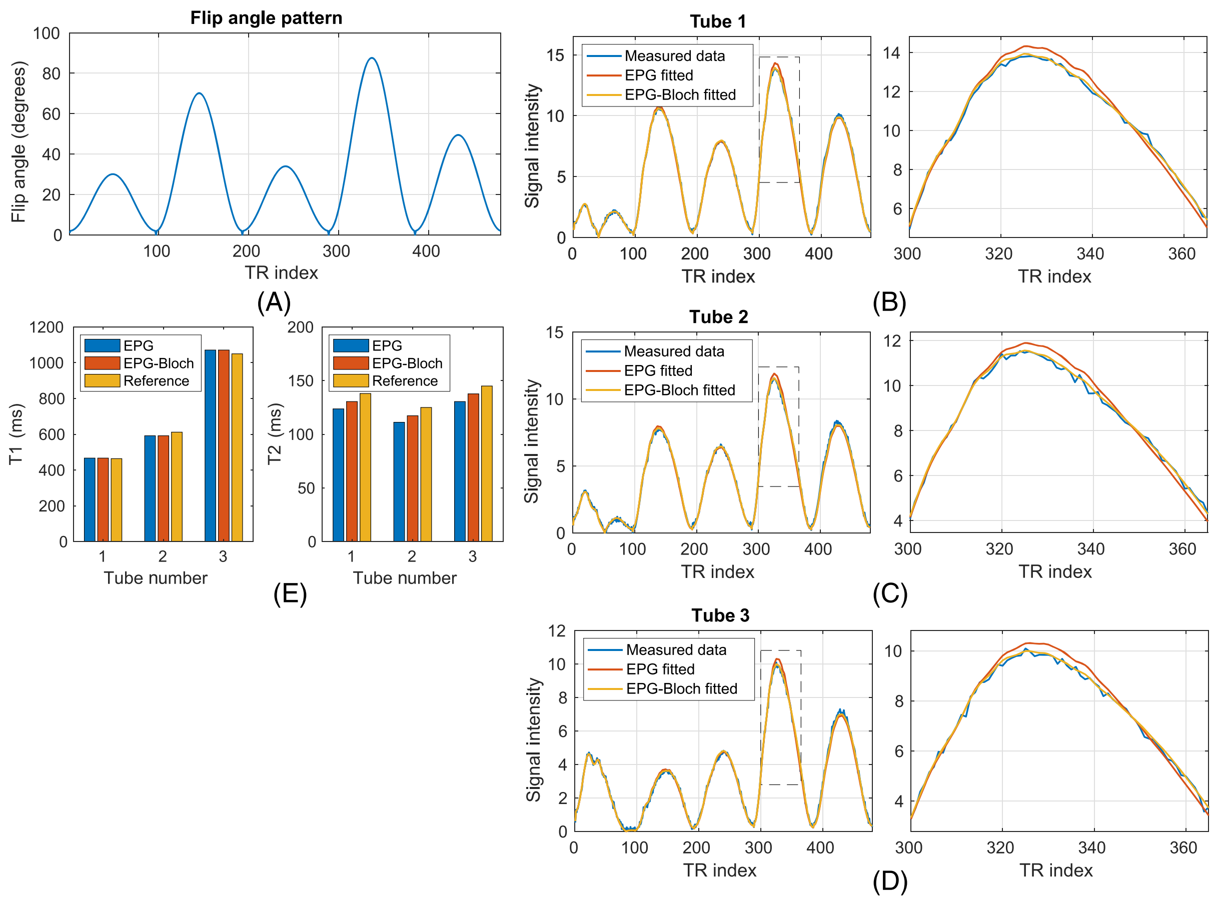

FIGURE 2 Experimental validation of the extended phase graph (EPG)-Bloch model. A, Flip-angle train for the transient-state gradient-spoiled sequence. B-D, Experimental data compared with both conventional EPG and EPG-Bloch results for the three tubes with different T_1 and T_2 values. A magnified portion is shown to the right of each plot. E, Fitted T_1 and T_2 values using conventional EPG and EPG-Bloch–generated dictionaries, compared with 2DMix reference results

3.2 | Training and validation of the RNN model

3.2.1 | Network structure specification

The RNN architecture described in Section 2.2 was selected for modeling gradient-spoiled sequence responses. Specifically, at the n-th time step, the inputs of the network were tissue parameters in logarithmic scale $\boldsymbol{\theta} = (\log T_1, \log T_2)^T$ and time-dependent sequence parameters $\boldsymbol{\beta} = (T_R(n), T_E(n), \alpha(n))^T$, and the outputs were $(M_{xy}(n), \partial M_{xy}(n)/\partial \boldsymbol{\theta})^T$, that is, both the magnetization and derivatives. At the first time step ($n = 0$), the input for the initial linear layer was the initial magnetization vector $\mathbf{M}_0 = (M_x(0), M_y(0), M_z(0))^T$. Each layer of the GRUs had 32 hidden states, and the whole network has in total 16,643 trainable parameters.

3.2.2 | Dataset generation

The training data were simulated from the newly proposed EPG-Bloch model, containing a total number of 30,000 magnetization signals. Each magnetization signal was simulated using a gradient-spoiled sequence with 1120 RF pulses, and all the RF pulses had a Gaussian waveform shape with a duration of 1.0 ms, and the same slice-selective and phase-refocusing gradients leading to a slice thickness of 3 mm.

In the training dataset, each magnetization signal was computed using different input parameters. For tissue parameters $\boldsymbol{\theta} = [\log T_1, \log T_2]^T$, T_1 and T_2 values were randomly sampled from logarithmic distributions ranging within 0.1–5.0 and 0.01–2 s, respectively. Only the parameter combinations with T_1 greater than or equal to T_2 were taken into account. For sequence parameters, T_R and T_E were chosen to be either time-constant or time-varying: for time-constant T_R and T_E, one T_R value was sampled uniformly within 5–20 ms for all RF pulses, and one $T_E(n)$ value from 0.3 x T_R–0.7 x T_R ms; for time-dependent T_R and T_E, T_R and T_E values were randomly sampled for each of the RF pulses following the same sampling rule as the time-constant condition. For the flip-angle train $\boldsymbol{\alpha} = [\alpha(1), \alpha(2), \ldots, \alpha(N_{TR})]^T$, every flip angle $\alpha(n)$ was constrained to be in the interval 0^o–120^o. The flip-angle trains used for training the RNN network were all different and were randomly sampled from five different types of trains, including spline-interpolated functions with five control points (*Spline5*), spline-interpolated function with 11 control points (*Spline11*), sine-squared function with five sinusoidal lobes (*SinSquared5*), spline-interpolated function with a superimposed pseudo-random Gaussian component (*SplineNoise11*) and piecewise-constant functions (*PieceConstant5*). Details about how to generate these five different types of flip-angle trains are included in the supporting information (Appendix B), and representative plots of the five types of waveforms are shown in Figure 3. In the dataset, each magnetization signal used a random flip-angle train generated from one of the five flip-angle train functions, so that the whole dataset had 6000 data signals generated using each type of the flip-angle trains for a total of 30,000 unique trains. These five types of flip-angle trains were either smoothly varying functions (*Spline5*, *SinSquared5*, *Spline11*), or smoothly varying functions with random components (*SplineNoise11*), or piecewise-constant functions with random jumps (*PieceConstant5*). They provided various inputs feeding into the model such that various physical dynamics of the EPG model could be learned. The initial magnetization $\boldsymbol{M}_0$ for the input of the initial linear layer was randomly chosen to be either $[0,0,-1]^T$ for a sequence with an initial inversion pulse or $[0,0,1]^T$ for a sequence without an inversion pulse.

To generate the training dataset, magnetization signals M_{xy} were simulated by the new EPG-Bloch model using the generated input parameters described in the previous paragraph, and derivatives of the signals $\partial M_{xy}/\partial \boldsymbol{\theta}$ were simulated by using automatic differentiation. In total, 20,000 data signals from the dataset were randomly selected for training the network coefficients, and the remaining 10,000 signals were used for testing.

3.2.3 | Network training and validation

The RNN network was built and trained using Tensorflow 2.2[40] on a Tesla V100 GPU with an Intel Xeon 2.6 GHz processor. The Tesla V100 GPU has a 32-GB memory but we limited the maximum memory usage to be 12 GB, to show that the network can be trained on lower end cards with less available GPU memory capacity. The training was run for 3000 epochs by an ADAM optimizer with adaptive learning rates,[41] with a batch size of 200. An L1 loss function, mean absolute error (MAE), was used during the training, and both MAE for the signal and its derivatives were weighted equally in the loss function.

The trained RNN model was subsequently used for predicting the magnetization and derivative signals with different tissue parameters and sequence parameters. The model was tested on the test data in the calculated dataset, and normalized root mean square errors (NRMSEs) were used as the evaluation metric, and were calculated separately for signals and derivatives with different types of flip-angle trains.

3.2.4 | Runtime evaluation

The trained RNN model can predict multiple signals in parallel in batches to accelerate the computation either on a CPU or GPU. The type of hardware used for running the models is reported between brackets in the runtime evaluation experiment; the RNN model is only run on a CPU for runtime evaluation experiments. For reconstruction-related experiments in later sections, the RNN model is always run on a GPU without additional specifications. A maximum batch size of 6400 was selected to limit the memory usage to no more than 12 GB. To evaluate the computational speed of the RNN (GPU) model prediction, different numbers of signals were predicted by the RNN model and the corresponding

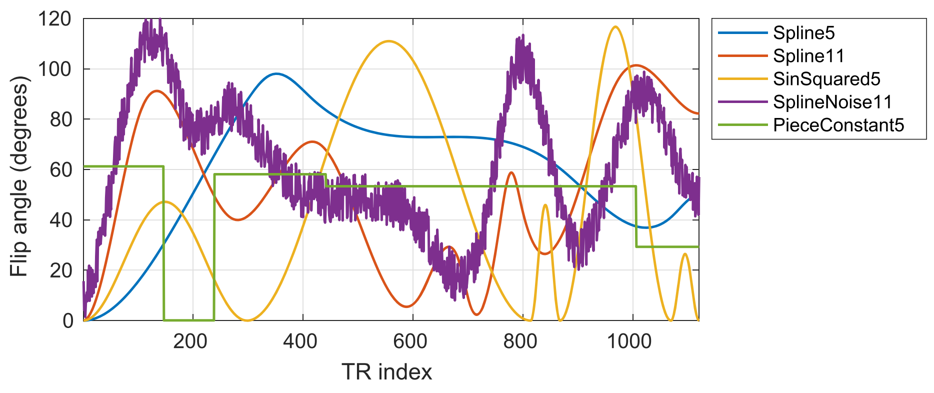

FIGURE 3 Example flip-angle trains for training the recurrent neural network (RNN)-extended phase graph (EPG) model. Five flip-angle trains sampled from each different type of train function are plotted

runtimes were recorded. Every magnetization signal has a length of $N_{TR} = 1120$, and is simulated given the same sequence parameters, as shown in Figure 4A. When the number of magnetization signals N_s was no larger than the maximum batch size 6400, we chose the batch size $N_{batch} = N_s$; otherwise we set $N_{batch} = 6400$.For performance comparison purposes, snapMRF (GPU),[12] the RNN (CPU) model and the proposed EPG-Bloch (CPU) model were all used for the runtime tests. SnapMRF is an open source package for dictionary generation and signal matching in MRF. It allows for fast parallelizable GPU execution, and both physical models, Bloch equation and EPG model, are supported for signal simulation. To conform the snapMRF results as equivalent to the EPG model with slice-profile correction, as described in Section 2.1, the snapMRF code needs to be repeated 32 times with different effective flip-angle trains. Note that snapMRF always treats RF excitation effects as instantaneous rotation, and therefore cannot be easily modified to realize EPG-Bloch model computations, thus we expect errors in the accuracy of the snapMRF model. Nonetheless, we decided to use snapMRF as it is publicly available and seems to be one of the best performing software packages in circulation.

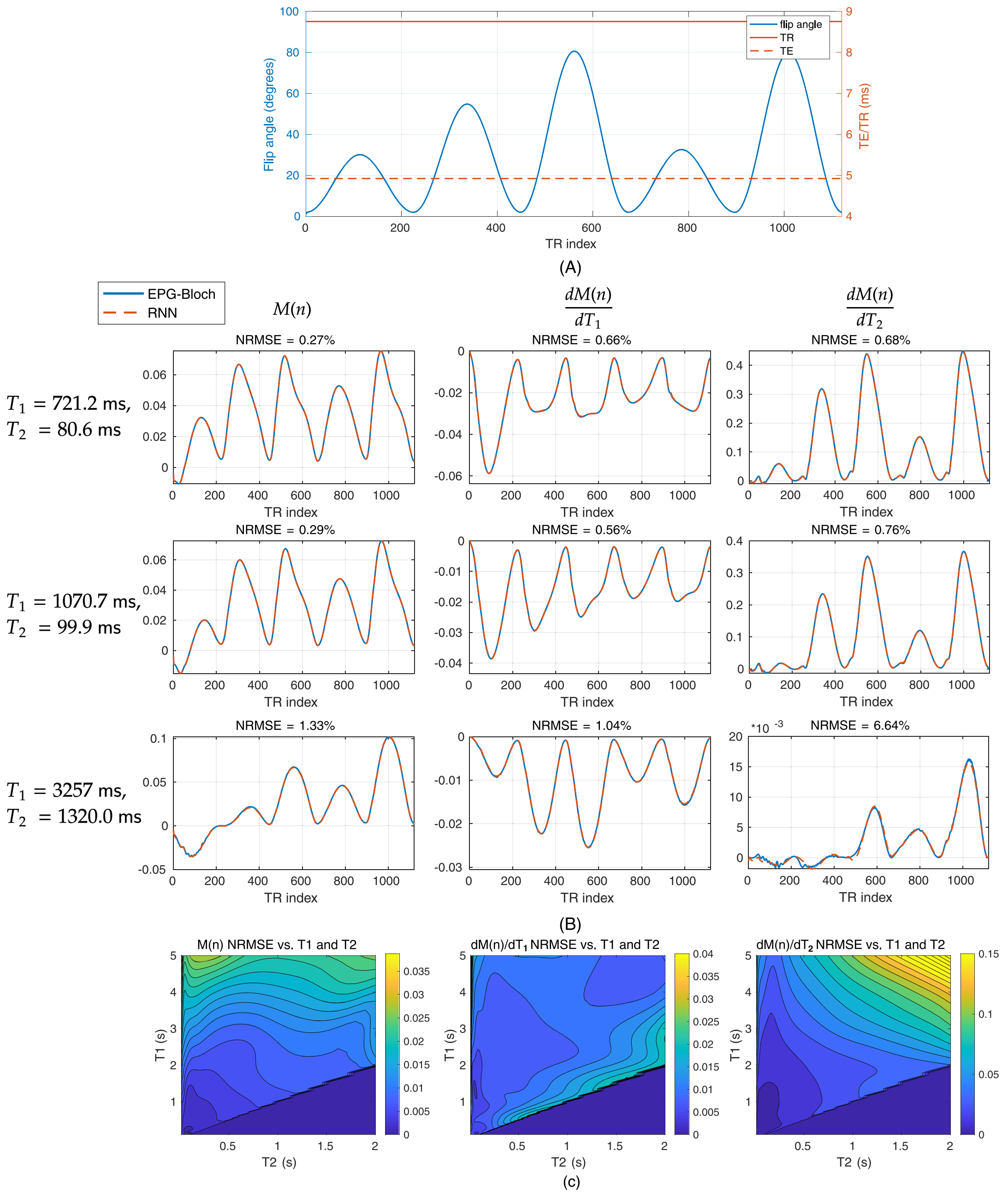

FIGURE 4 Sample magnetization and derivative signals generated with the surrogate recurrent neural network (RNN) model. A, Sequence parameter (flip-angle train, time-constant TE and TR) plots. Initial magnetization is $M_0 = [0,0,-1]^T$ after the inversion pulse. B, Magnetization signal and derivative plots compared with extended phase graph (EPG)-Bloch results given different T_1 and T_2 values. C, Contour images of normalized root mean square errors (NRMSEs) of RNN in reference to EPG-Bloch against the ranges of simulated T1 and T2 values

Two different experiments were run for testing the runtime with respect to the number of signals. For fixed $B_1^+ = 1.0$, six different discretizations of the T_1 and T_2 domain were selected, resulting in a two-dimensional dictionary of $N_s = 100,400,800,1600,3200,6400$ signals. For the case with various B_1^+ inputs, four different discretizations were selected for B_1^+, T_1 and T_2, respectively, such that the number of different B_1^+ values would be 10, 20, 40 and 80, and the total number of signals in the three-dimensional dictionary was $N_s = 10^3,20^3,40^3,80^3$. For the varying B_1^+ case, only snapMRF (GPU) and RNN (GPU) were tested since the runtime for the other two CPU models would be prohibitively long. We noted that computation of the derivatives by the proposed RNN (GPU) model does not significantly increase the computation time since it only requires a small last linear step. For this reason, no explicit timing tests were run for the derivative parts. For the RNN (CPU/GPU) model, computations in the last linear layer (the box at the top of Figure 1A) related to signal derivatives can be removed when no derivatives are required.

3.3 | Applications of the RNN model

3.3.1 | MRF reconstruction using an RNN-generated dictionary

Numerical brain phantom

To test the performance of the trained RNN model, the model was used for fast MRF dictionary generation. A gradient-spoiled, transient-state sequence was used with the sequence parameters, as shown in Figure 4A. One radial k-space spoke with a golden-angle increment[42] was acquired for each TR with 224 sampling points along each readout spoke.

An MRF dictionary was generated by the surrogate RNN model with 100 logarithmically spaced T_1 values within 0.1–5 s, 100 logarithmically spaced T_2 values within 0.01– 2 s and 40 uniformly spaced B_1^+ values within 0.8–1.2 a.u. This resulted in a dictionary with 312,480 atoms after the cases, for which T_2 greater than T_1 were removed. For comparison, a second MRF dictionary was also generated with the EPG-Bloch model using the same reconstruction parameter values.

A numerical brain phantom[43] with a matrix size of 112×112 was used to simulate the synthetic data. To avoid the appearance of any "inverse crime", a multispin comprehensive Bloch simulation[28] was used to compute the magnetization signal for each voxel. Specifically for each MR signal simulation, 6400 spatial points were sampled, both along the in-plane direction and along the slice-selective direction, in order to model the slice-profile effects and the intravoxel dephasing effects by in-plane and through-plane spoiling gradients. The acquired k-space data were then simulated by applying the nonuniform Fourier transform to the volumetric magnetization signal. A receive array of 13-coil was simulated to obtain the multicoil k-space data, and complex Gaussian noise was then added to the simulated k-space data with a noise level SNR of 20. The SNR was defined by the average k-space signal intensity divided by the standard deviation of the noise. T_1, T_2, B_1^+ and PD maps were reconstructed by the low-rank alternating direction method of multipliers (LR-ADMM) approach[44] using either the RNN-generated or EPG-Bloch–generated dictionary. Four virtual coil data compressed from the 13-coil–simulated data by singular value decomposition (SVD) were used for the reconstruction. The reconstruction parameters in the LR-ADMM algorithm were: rank $R = 12$, ADMM penalty parameter $\mu = 0.015$, outer ADMM iterations $= 20$ and inner CG iterations $= 10$.

In vivo data

In vivo experimental data were collected on the 3.0-T MR system (Ingenia, Philips Healthcare) using the same sequence as in the previous numerical experiment. The same reconstruction parameters were used, except that a homogenous $B_1^+ = 1.0$ was assumed and excluded from MRF reconstruction, and only six ADMM iterations were used to avoid overfitting during the LR-ADMM reconstructions.

3.3.2 | Accelerating the optimal experimental design for the MRF sequence

In statistical data analysis, the CRLB gives a lower bound on the variance of an unbiased estimator of a parameter,[45] which is derived by inversion of the Fisher information matrix (FIM). The FIM is constructed by computing the derivatives of the signal with respect to the parameters to be estimated. The CRLB has been used for optimizing MRF sequence parameters for a small number of tissues with given T_1 and T_2 values.[20,21,46] For such an optimal experimental design problem, the objective function can be defined in several ways, depending on the criterion under consideration. A popular choice is to consider the weighted sum of the trace of the CRLB matrix. Optimizing CRLB objectives can be very computationally inefficient, because it requires computing a large number of magnetization signals and their derivatives, and it might even require the computation of the objective function's derivatives with respect to sequence parameters when using derivative-based optimization algorithms.[47]

In this application, the RNN model was used for developing a computationally efficient method to optimize a gradient-spoiled MRF sequence. Given various sequence parameters, the RNN model is capable of computing large amounts of magnetization signals and derivative signals with respect to tissue parameters, and therefore is highly suitable for solving the CRLB optimization problem for optimal sequence design. For this aim, we departed from the standard derivative-based optimization algorithms, which are prone to find suboptimal solutions given the nonconvexity of the objective, and we chose to use a derivative-free, population-based optimization method[46] instead. In particular, we use the differential evolution (DE),[48,49] an algorithm which iteratively evolves the candidates in the population to obtain an improved solution in a derivative-free fashion. Note that here, by "derivative-free" we mean that the derivative of the objective function is not required during the optimization; however, in the CRLB-based optimal design problem, the objective function itself still requires derivative computation with respect to target tissue parameters. The code for solving this optimal experimental design problem is implemented in Python using the DE algorithm in Scipy and the trained RNN model.

Specifically, we conducted a simulation-based experiment to optimize the flip-angle train of an MRF sequence given two target tissues with $T_1/T_2 = 900/85$ ms and $T_1/T_2 = 500/65$ ms. For sequence parameters, we used time-constant $T_E/T_R = 4.9/8.7$ms and $N_{TR} = 336$ (a different sequence length from the training data) with an initial inversion pulse, resulting in a very short acquisition time of 2.92 s. The flip-angle train to be optimized was constrained to be only a *Spline11* (see Appendix B) type waveform and the maximum flip angle to be 90 degrees. The constrained DE implementation provided by SciPy v. 1.5.0[50] was modified and used for solving the optimization problem. In each iteration of the modified DE algorithm, the RNN model was used once for computing the magnetization signals and derivatives for the whole population very quickly. For the DE optimization, we set the population size to be equal to 10. Since *Spline11* requires 11 parameters to compute a complete flip-angle train and two target tissues are to be optimized, in each iteration a maximum of $10 \times 11 \times 2 = 220$ magnetization and derivative signals need to be computed. Other algorithm parameters using nondefault values include: relative tolerance for convergence = 0.002, and maximum number of generations = 1000.

To evaluate the optimization results, two MRF reconstructions, with the original flip-angle train (made of the first 336 TRs shown in Figure 4A) and the optimized one, were conducted using the RNN-generated dictionaries. The same numerical brain phantom, data-generation method, and reconstruction algorithm, as described in Section 3.3.1, were used with only one main difference: to reduce the effects of k-space undersampling, a spiral acquisition was used. The same spiral trajectory as in references[6,20] was used and one interleaf of a variable density spiral trajectory was acquired for each TR, whereas 48 interleaves were required for fully sampling the k-space. An ideal $B_1^+ = 1$ field was assumed everywhere and therefore it was not included in the MRF reconstructions.

4 | RESULTS

4.1 | Validation of the new EPG model

Figure 2B–D compares the experimentally measured data with both the conventional EPG and the proposed EPG-Bloch model predictions. For larger flip-angle segments (around the 336th TR index), as shown in the right column of magnified figures, simulated signals by the conventional EPG model are significantly larger than the measured data, while the new EPG-Bloch model signals show an improved match. The simulation runtime for one single signal using the EPG-Bloch model was 0.34 s, which was about 10 times slower than using the EPG model (0.032 s). The reconstructed T_1 and T_2 values from using both EPG models are summarized in Figure 2E. For each of the three gel tubes, the fitted T_2 values by the new EPG-Bloch model are all slightly higher (about 10 ms) than the fitted T_2 values by the conventional EPG model, and are closer to the measured reference values by the reference sequence. The fitted T_1 values by both models show relatively small differences, and are both in good agreement with measured reference values. In this experiment, the better accuracy of the newly proposed EPG-Bloch model is proven, motivating the use of this accurate but computationally more expensive EPG-Bloch model for quantitative MR methods.

4.2 | Validation of the RNN model

4.2.1 | Network validation results

The total training time was approximately 8 h, and the overall results for the RNN model validation are summarized in Table 1. The NRMSEs for five different types of flip-angle trains are given for the signals and derivatives, respectively. This shows that the RNN results agree well with the EPG-Bloch results. The RNN results are less accurate for *PieceConstant5* flip-angle trains compared with the other types. This problem may be solved by increasing the portion of the *PieceConstant5* type data used for training, which is 20% for the original whole training set. Since this type of train is not common in transient state acquisitions, we did not perform additional trainings.

Two examples of sample magnetization and derivative signals generated from RNN are shown in Figures 4 and 5. Figure 4A illustrates the sequence parameters used for a flip-angle train that belongs to the *SinSquared* type. Figure 4B shows RNN-generated magnetization and derivatives for different T_1 and T_2 values. The three combinations of T_1 and T_2 values are chosen to be close to white matter, gray matter and cerebrospinal fluid (CSF) tissue parameters. All these RNN results are well matched with the EPG-Bloch results. Figure 5 shows similar results to Figure 4.

TABLE 1 Validation of the recurrent neural network (RNN)- extended phase graph (EPG) model for different types of flip-angle trains. Normalized root mean square error (NRMSE) are computed for the validation dataset. Errors are computed respectively for data with different types of flip-angle trains, and signal and derivative errors are computed separately

	Spline5	*Spline11*	*SinSquared5*	*SplineNoise11*	*PieceConstant5*
Signal	0.418%	0.574%	0.780%	1.285%	5.155%
Derivative	0.801%	1.008%	1.694%	2.037%	3.913%

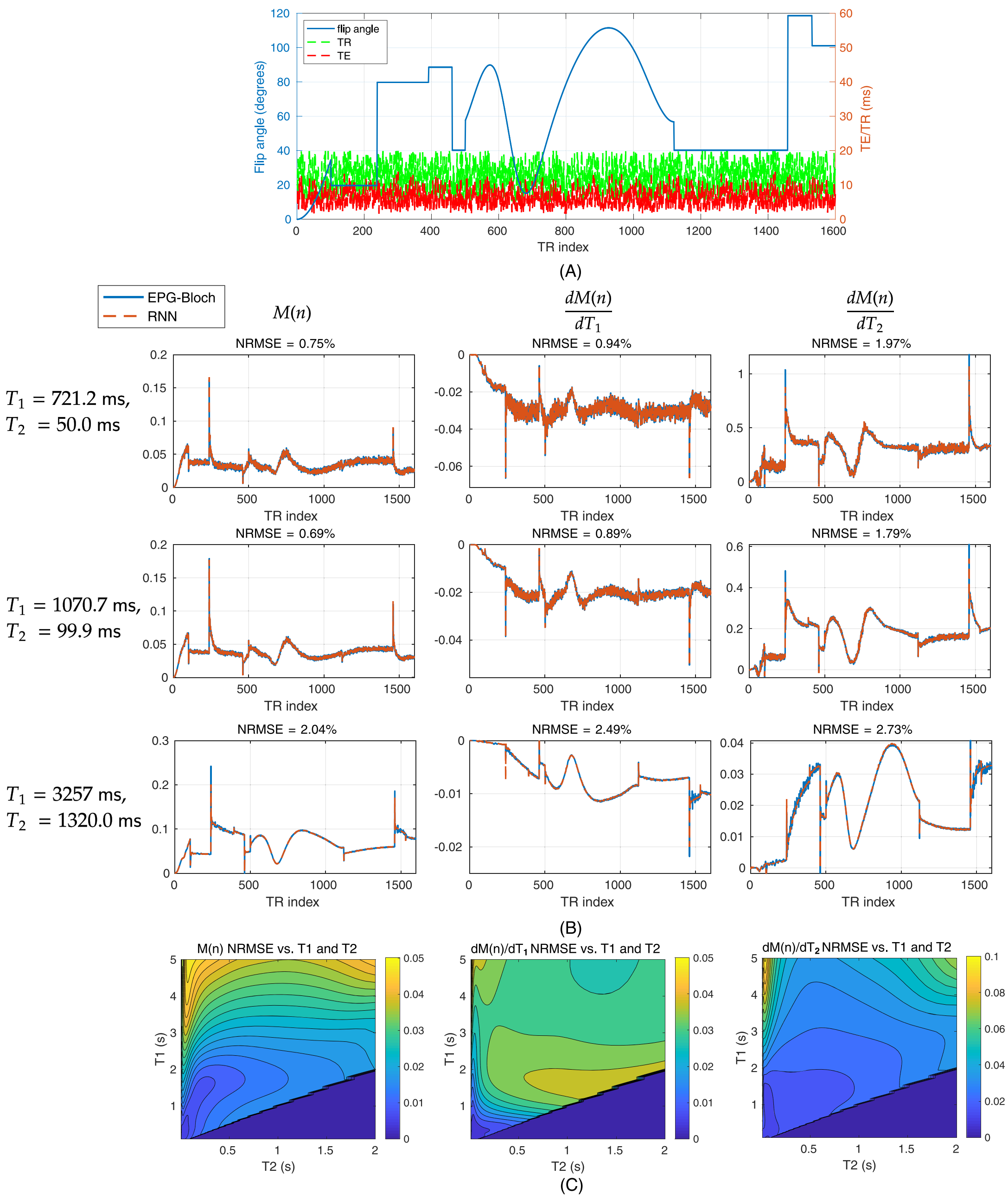

FIGURE 5 Another sample magnetization and derivative signals generated with the surrogate recurrent neural network (RNN) model. A, Sequence parameter (flip-angle train, time-varying TE and TR) plots. No inversion pulse is applied. B, Magnetization signal and derivative plots compared with extended phase graph (EPG)-Bloch results given different T_1 and T_2 values. C, Contour images of normalized root mean square errors (NRMSEs) of RNN in reference to EPG-Bloch against the ranges of simulated T1 and T2 values

However, the sequence used here is longer than the ones used for training, and the flip-angle train is a combination of *Spline11* and *PieceConstant5* types, and which is not included in the training dataset. The RNN results are still well matched with the EPG-Bloch results, showing good generalization properties of the trained RNN model. Figures 4C and 5C show the contour images of NRMSEs of the RNN with reference to EPG-Bloch against the ranges of simulated T1 and T2 values for the two different sequences, and overall they show relatively low signal and derivative errors for various tissue parameters.

Runtime evaluation

Figure 6 shows the runtime comparison results for the RNN (GPU) and snapMRF (GPU). As shown in both Figure 6A,B, all the runtime curves grow approximately linearly with respect to the number of signals. For the fixed B_1^+ condition in Figure 6A, RNN (GPU) requires approximately 100 times less runtime than snapMRF (GPU) for a dataset with 6400 signals, and approximately 200 times less runtime than the RNN (CPU) model and approximately 34,000 times less than the EPG-Bloch (CPU) model. For the various B_1^+ conditions in Figure 6B, RNN (GPU) outperforms snapMRF (GPU) by a factor of 68 for a large dataset with 512,000 signals.

The runtime comparison is divided into a fixed B_1^+ condition and various B_1^+ conditions, because the kernels in snapMRF are not parallelized for datapoints with different B_1^+ values. For example, snapMRF takes 144 s for a dataset of 6400 signals with 20 different B_1^+ values, but only takes 15.7 s for the same size of dataset with one fixed B_1^+ value. However, for the RNN (CPU/GPU) model, B_1^+ values and tissue parameter inputs do not affect the runtime. The RNN runtime is only affected by the number of signals and the sequence length N_{TR}. Note that the acceleration rate of the RNN (GPU) model compared with snapMRF (GPU) slightly decreases for a larger number of signals, but the RNN (GPU) model still performs much faster, because of the repetitive computations required by the slice-profile correction in snapMRF.

4.3 | Applications of the RNN-EPG model

4.3.1 | MRF reconstruction using an RNN-EPG–generated dictionary

Numerical brain phantom

MRF reconstruction results using dictionaries generated by different models are shown in Figure 7. Mean relative errors are shown in the upper right corner of each relative error map. Using the EPG-Bloch and RNN model-generated dictionaries, the reconstructions show high agreement with the ground truth maps, with the surrogate RNN model results having slightly higher relative errors compared with the EPG-Bloch model. By contrast, using the conventional EPG model-generated dictionary, the T_2, B_1^+ and *PD* maps are poorly reconstructed: overall, underestimated T_2 values are observed, and the B_1^+ map reconstruction fails.

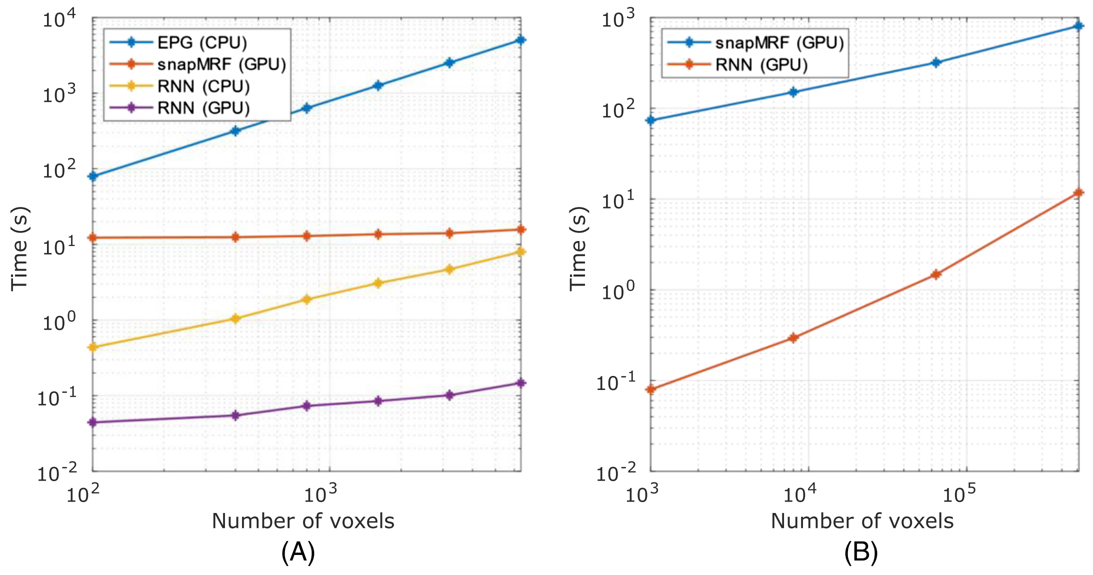

FIGURE 6 Recurrent neural network (RNN) (graphics processing unit [GPU]) runtime comparisons with snapMRF (GPU), RNN (central processing unit [CPU]) and extended phase graph (EPG) (CPU). A, Runtime comparison for the two-dimensional (T_1,T_2) dictionary generation. B, Runtime comparison for the three-dimensional (T_1,T_2,B_1^+) dictionary

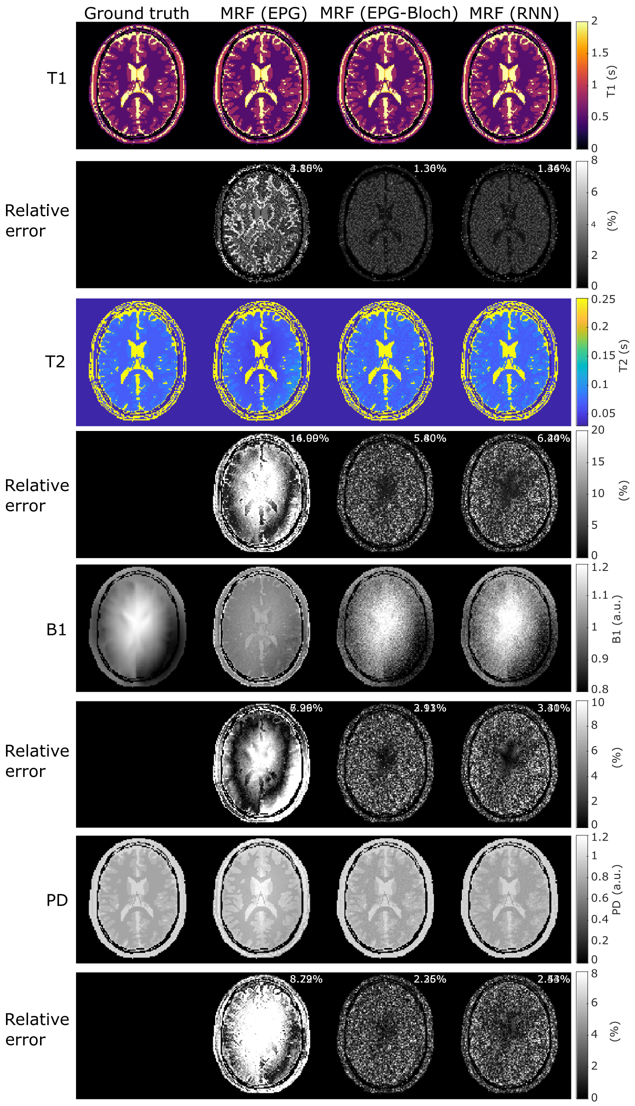

FIGURE 7 Magnetic resonance fingerprinting (MRF) reconstructions of the numerical brain phantom for different signal models. Mean absolute percentage error (MAPE) values are reported on the error maps. First column, Ground truth T_1, T_2, B_1^+ and *PD* maps for the numerical brain phantom. Second, third and fourth columns, Reconstructed maps and absolute relative error maps for MRF using different dictionaries. Second column, MRF dictionary generated by the original extended phase graph (EPG) model with small tip-angle approximation. Third column, MRF dictionary generated by the new EPG-Bloch model. Fourth column, MRF dictionary generated by the recurrent neural network (RNN) model. Both the EPG-Bloch and RNN reconstruction results show great agreement with the ground truth maps, with the RNN results having slightly higher relative errors, whereas the MRF (EPG) results have relatively high reconstruction errors, especially for the T_2, B_1^+ and *PD* maps

For these numerical experiments, three reconstruction parameters, T_1, T_2 and B_1^+, are included, resulting in a dictionary with 312,480 atoms. Generating the whole dictionary using the EPG-Bloch model on a CPU takes about 71 h; however, dictionary generation using the RNN model on a GPU takes less than 10 s. This indicates the extreme efficiency of using the RNN model for MRF dictionary generation with negligible loss in image quality.

In vivo data

MRF reconstruction results using in vivo data are shown in Figure 8. The mean absolute differences between EPG-Bloch reconstruction and RNN reconstruction are 1.74%, 3.46% and 2.02% for T_1, T_2 and abs (*PD*) maps, respectively, and relatively larger differences mostly exist in CSF regions. Differences between EPG and RNN reconstruction are relatively large, which is consistent with the results in Figure 7. We plot and compute the mean absolute differences for the absolute PD, because the phase information is usually not relevant for PD maps.

4.3.2 | Accelerating the optimal experimental design for the MRF sequence

The flip-angle train obtained after solving the optimal experimental design problem described in Section 3.3.2 is shown in Figure 9A. Compared with previously reported results,[20,21] the optimized flip-angle train shows a very similar smoothened trapezoidal pattern. Solving this optimization problem requires about 120 iterations to converge using the DE algorithm for a total of approximately 14,000 signal derivative computations by the RNN model. The total runtime is 9.8 s when using the RNN model. In previous work,[20,21] similar optimal experimental design problems have

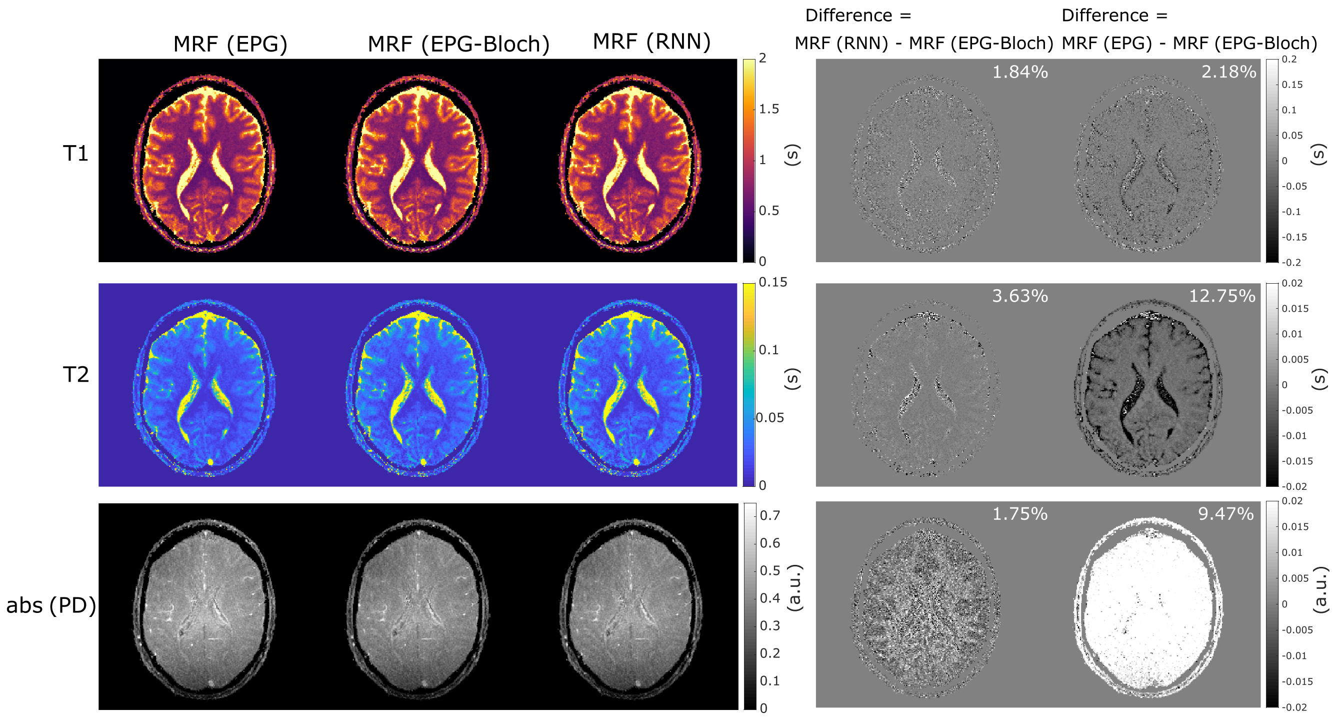

FIGURE 8 Magnetic resonance fingerprinting (MRF) reconstructions of in vivo data using extended phase graph (EPG), EPG-Bloch and recurrent neural network (RNN) generated dictionaries. First, second and third rows, T_1, T_2, and PD maps for the in vivo brain data

required at least 1 h of CPU time to solve. Our proposed implementation using the RNN model shows a significantly reduced runtime by approximately two orders of magnitude.

Figure 9B shows the MRF-reconstructed T_1, T_2 and PD maps using the original and optimized flip-angle trains. It can be seen that the optimized sequence improves the accuracy of all the three reconstructed maps compared with the original sequence, and the improvement in T_2 maps is the most significant.

5 | DISCUSSION

In this work, we have presented a new EPG-Bloch model that accurately models the RF excitation effects. For the EPG-Bloch model, rotation operations are applied in the configuration state domain to compute RF pulse excitations by sequentially discretized substeps, similar to computing RF pulse excitation effects in the spin domain using the Bloch equation. The effects of other components of the sequence (e.g. the spoiler gradients) are simulated in the configuration state domain. By applying the new EPG-Bloch model, more accurate magnetization signals can be computed by tracing the signal evolution of just 15–20 configuration states. By comparison, the conventional EPG model using the slice-profile correction method is less accurate, especially when larger flip angles are employed. Note that a full Bloch equation model using multiple isochromats can also be applied for computing the gradient-spoiled sequences, but is less computationally efficient compared with the new EPG-Bloch model. Theoretically, to fully simulate a gradient-spoiled sequence, one would need the same number of configuration states N_k in EPG simulation as the number of isochromats N_{iso}in the Bloch simulation, that is, $N_k = N_{iso} = N_{TR}$.[37] However, in practice, since the configuration states in the EPG model decay through time as a consequence of spin-spin and spin-lattice relaxation, N_k can be substantially lower than N_{TR}, thus the number of configuration states required by the EPG model is much smaller than the number of spatial isochromats required by the Bloch simulator to achieve accurate simulation.[28,37] In conclusion, we combined the best ingredients of both models (Bloch and EPG) into a combined model that is faster than the Bloch simulation and more accurate than the conventional EPG simulator. Recent work[51] has also incorporated the time-dependent RF waveform response for accurate modeling of the slice-profile effects (the ssEPG model). In ssEPG, the RF excitation is simulated in the configuration space (frequency domain) along the slice-selective dimension, whereas in our EPG-Bloch model we propose to simulate the RF excitation separately for each subslice (space domain). Both models seem to agree very well with experimental measurements and are more accurate alternatives to the standard EPG. Extended comparison of the two methods would go beyond the scope of this work and is left to future work. It should be noticed that, similar to EPG-Bloch, the ssEPG model is also computationally slower than conventional EPG, indicating the necessity for acceleration. The latter is an additional motivation for the main contribution of this paper, that is, acceleration by RNN surrogates.

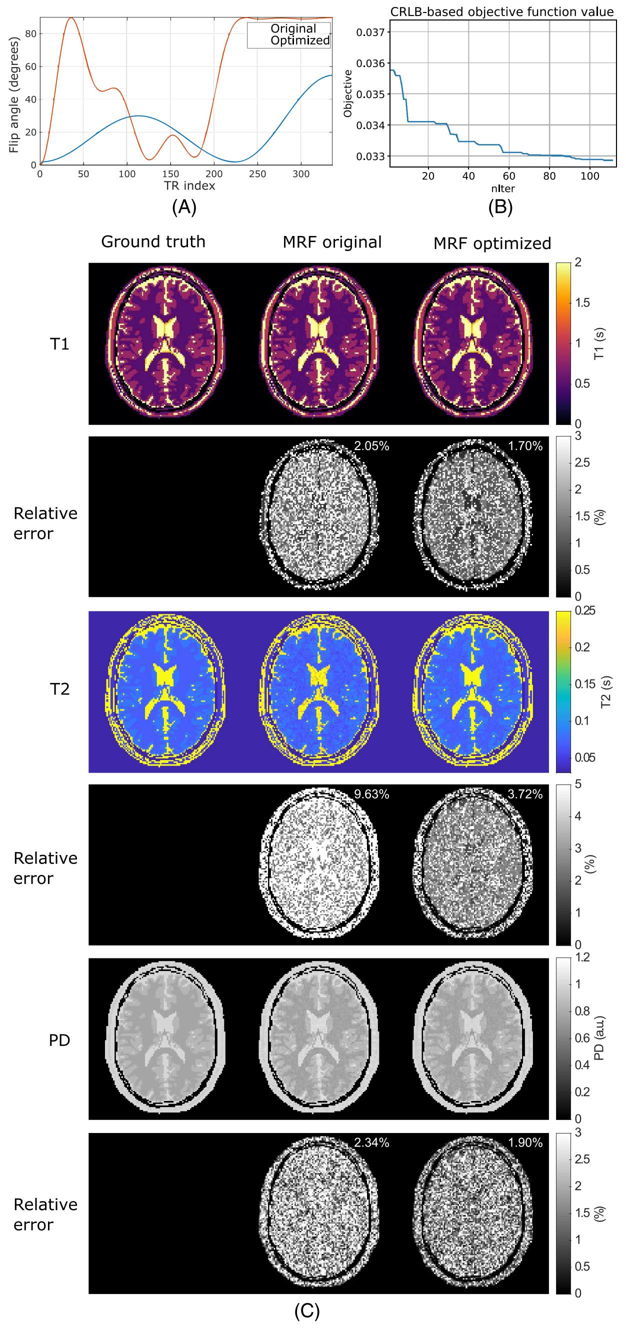

FIGURE 9 Optimal numerical experimental design results. A, The original and optimized flip-angle trains. B, Convergence curve for optimal experimental design problem using a differential evolution (DE) algorithm. Objective function is reported as a function of iteration number (nIter). C, Magnetic resonance fingerprinting (MRF) reconstruction results using the two different flip-angle trains. First column, Ground truth T_1, T_2 and PD maps for the numerical brain phantom. Second and third columns, Reconstructed MRF maps and absolute relative error maps obtained using, respectively, the original and the optimized flip-angle trains. Mean absolute percentage error (MAPE) values are reported in the upper right corner of the error maps. Note the enhanced accuracy that is obtained with the optimized flip-angle train, especially for T_2 reconstructions, CRLB, Cramér–Rao lower bound

One main advantage of the RNN model is its generalization capability, since it is able to learn MR signals for various sequence parameters, such as flip-angle training, repetition time and sequence length. After training with a relatively small dataset with 20,000 MR signals, which takes 13 h of CPU time to generate, the RNN model could compute magnetization signals for sequences with new sequence parameters (e.g. new time-varying flip-angle trains) without the need for retraining. This suggests that the RNN model could be used for fast signal computations when sequences need to be modified. For example, experimental results in the supporting information (Appendix C) show that the RNN model could be used for simulating different new MR sequences, such as extremely long sequences, or sequences with flip-angle train patterns not included in the training dataset. The RNN model can also be used for accelerating the sequence parameter optimization process, when signal and derivatives for different sequence parameters need to be computed. Our numerical experiment results show that optimizing a flip-angle train of length 400 for two target tissues requires only 41 s when run on a GPU, and may be further used for accelerating more complicated sequence optimization problems in the future, for example, optimizing sequences for more reconstruction parameters, such as magnetization transfer[52] or B_1^+.

The main purpose of using the RNN model is to accelerate large-scale MR signal computations. When run on a GPU, the proposed RNN model requires at the most 10 s to generate a large MRF dictionary with 2 x 10^5 magnetization signals. Training the RNN requires a relatively small training dataset with 2 x 10^4 magnetization signals, only 10% of the size of the dictionary, and takes a relatively long training time, in our experiment more than 8 h for 3000 epochs. Generation of the training dataset by the EPG-Bloch model also adds about another 13 h of computation time. However, dataset generation and network training need to be performed only once, the trained network requires very little storage space, and can be repeatedly loaded and used for signal computations with various tissue parameters and sequence parameters each time.

Another advantage of the proposed RNN model is that it can compute both the magnetization signal and the signal derivatives with respect to the parameters of interest (T_1 and T_2 in the current experiments) simultaneously. For the RNN model, derivatives can also be computed by using either the FD method or AD; however, the runtime would be at least doubled to also include the derivative computation. By contrast, we train our RNN model to compute both signal and derivative at the same time, such that the hidden states of the RNN units contain the derivative information, and the derivatives can be computed by a weighted sum of the hidden states. Our proposed RNN model requires negligible additional runtime for derivative computation.

The current RNN model learns the signal evolution for a gradient-spoiled sequence with a Gaussian RF excitation pulse. Since RNN architecture is very effective for learning various time-dependent processes, especially those which can be exactly modeled by ordinary differential equations, we believe the proposed RNN model is also able to learn different types of sequences, such as a gradient-spoiled sequence with a different RF shape, RF spoiled sequences or balanced sequences, or different physical models, such as presented in Ostenson et al.[51] Retraining for learning new types of sequences or other physical models will be required, but future training can be accelerated by transfer learning approaches[53] in the machine learning field, in which knowledge learned from previous trainings can be applied to a new but related problem. We have not performed experiments on bSSFP sequences yet. However, we did try to train the RNN for spoiled GRE sequences with different sinc-shape RF excitation pulses. When switching to a new RF pulse shape, using the already trained RNN as a warm start did expedite the training process, requiring just about 300 epochs to reach a similar accuracy as the previous 3000-epoch training.

The currently trained RNN model can compute MR signals for various sequence parameter inputs and initial conditions. For flip-angle train inputs, five different types of waveforms were used, including all commonly used patterns for qMRI applications, and many flip-angle trains outside these five types can still be accurately computed. For repetition time inputs, T_R can be either constant or time-varying in a random fashion throughout the sequence. For initial magnetization, two different initial values, either $[0,0,-1]^T$ for perfect inversion pulse at the beginning or $[0,0,1]^T$ for no inversion pulse, were used. The currently used RNN architecture has three stacked GRU layers for one time-step computation, with 32 hidden states in each layer. Since the EPG-Bloch model is highly nonlinear, stacking multiple RNN units per time step helps model the nonlinearity more accurately. In principle, an arbitrary number of RNN units can be stacked. However, experimental results show that using one or two GRU layers and less hidden states leads to poorer accuracy, and adding more stacked units or hidden states leads to a longer computational time without significant improvements in model accuracy. Therefore, the currently used architecture is an empirical choice considering both aspects. In the future, to train an RNN model for more sequence parameter and initial magnetization inputs, exploration of new network architectures may be required.

RNNs are relatively sequential to compute the signal for each time step, and they have very good generalization properties. However, our RNN model is less computationally efficient than other existing deep learning approaches. For example, it is reported in Hamilton et al.[15] that generating an MRF dictionary of size 1000 by 5930 takes 0.3 s on a CPU. Generating an MRF dictionary of the same size using the RNN model takes 7.2 s on a similar CPU. Further acceleration of the RNN model may be achieved by using more powerful computer capacity and state-of-the-art RNN inference libraries.[54]

6 | CONCLUSION

This work proposed a new EPG-Bloch model for simulating transient-state, gradient-spoiled MR sequences, and trained an RNN as a fast surrogate of the EPG-Bloch model for large-scale signal computations. By comparisons with measured phantom data, we showed that the proposed EPG-Bloch model is more accurate than the standard EPG with STA approximation for imperfect slice-profile correction. We further demonstrated that the RNN (EPG) model is computationally very efficient, at least four orders of magnitude faster than the EPG-Bloch simulation, and between one and three orders of magnitude faster than the GPU-accelerated EPG package, snapMRF. Example experiments demonstrated that the RNN model can be efficiently used for computing large-scale (>10^5) MR signal dictionaries and derivatives for different qMRI applications such as MRF within tens of seconds.

ACKNOWLEDGEMENTS

The authors are grateful to Tom Bruijnen for fruitful discussions. The first author (HL) receives a scholarship granted by the China Scholarship Council (CSC, #201807720088).

ORCID

Hongyan Liu https://orcid.org/0000-0002-1319-0419

REFERENCES

1. Filo S, Shtangel O, Salamon N, et al. Disentangling molecular alterations from water-content changes in the aging human brain using quantitative MRI. *Nat Commun.* 2019;10(1):1-16.
2. Piredda GF, Hilbert T, Granziera C, et al. Quantitative brain relaxation atlases for personalized detection and characterization of brain pathology. *Magn Reson Med.* 2020;83(1):337-351.
3. Ma D, Gulani V, Seiberlich N, et al. Magnetic resonance fingerprinting. *Nature.* 2013;495(7440):187-192.
4. Sbrizzi A, van der Heide O, Cloos M, et al. Fast quantitative MRI as a nonlinear tomography problem. *Magn Reson Imaging.* 2018;46:56-63.
5. Weigel M. Extended phase graphs: dephasing, RF pulses, and echoes-pure and simple. *J Magn Reson Imaging.* 2015;41(2):266-295.
6. Jiang Y, Ma D, Seiberlich N, Gulani V, Griswold MA. MR fingerprinting using fast imaging with steady state precession (FISP) with spiral readout. *Magn Reson Med.* 2015;74(6):1621-1631.
7. van der Heide O, Sbrizzi A, Bruijnen T, van den Berg CAT. Extension of MR-STAT to non-Cartesian and gradient-spoiled sequences. In: *Proceedings of the 2020 Virtual Meeting of the ISMRM*; 2020:0886.
8. Mandija S, D'Agata F, Liu H, et al. A five-minute multi-parametric high-resolution whole-brain MR-STAT exam: first results from a clinical trial. In: *Proceedings of the 2020 Virtual Meeting of the ISMRM*; 2020:0558.
9. Davies M, Puy G, Vandergheynst P, Wiaux Y. A compressed sensing framework for magnetic resonance fingerprinting. *SIAM J Imaging Sci.* 2014;7(4): 2623-2656.
10. Serrao EM, Kessler DA, Carmo B, et al. Magnetic resonance fingerprinting of the pancreas at 1.5 T and 3.0 T. *Sci Rep.* 2020;10(1):1-11.
11. Körzdörfer G, Jiang Y, Speier P, et al. Magnetic resonance field fingerprinting. *Magn Reson Med.* 2019;81(4):2347-2359.
12. Wang D, Ostenson J, Smith DS. snapMRF: GPU-accelerated magnetic resonance fingerprinting dictionary generation and matching using extended phase graphs. *Magn Reson Imaging.* 2020;66:248-256.
13. Xanthis CG, Aletras AH. coreMRI: A high-performance, publicly available MR simulation platform on the cloud. *PLoS One.* 2019;14(5):e0216594. https://doi.org/10.1371/journal.pone.0216594
14. Yang M, Jiang Y, Ma D, Mehta BB, Griswold MA. Game of learning Bloch equation simulations for MR fingerprinting. *arXiv Prepr arXiv200402270*; 2020.
15. Hamilton JI, Currey D, Griswold M, Seiberlich N. A neural network for rapid generation of cardiac MR fingeprinting dictionaries with arbitrary heart rhythms. In: *Proceedings of the 27th Annual Meeting of ISMRM, Montreal*; 2019:2421.
16. Banerjee K, Georganas E, Kalamkar DD, et al. Optimizing deep learning rnn topologies on intel architecture. *Supercomput Front Innov.* 2019;6(3):64-85.
17. Chetlur S, Woolley C, Vandermersch P, et al. cudnn: Efficient primitives for deep learning. *arXiv Prepr arXiv14100759*; 2014.
18. Appleyard J, Kocisky T, Blunsom P. Optimizing performance of recurrent neural networks on gpus. *arXiv Prepr arXiv160401946*; 2016.
19. Sbrizzi A, Bruijnen T, van der Heide O, Luijten P, van den Berg CAT. Dictionary-free MR Fingerprinting reconstruction of balanced-GRE sequences. *arXiv Prepr arXiv171108905*; 2017.
20. Zhao B, Haldar JP, Liao C, et al. Optimal experiment design for magnetic resonance fingerprinting: Cramer-Rao bound meets spin dynamics. *IEEE Trans Med Imaging.* 2018;38(3):844-861.
21. Lee PK, Watkins LE, Anderson TI, Buonincontri G, Hargreaves BA. Flexible and efficient optimization of quantitative sequences using automatic differentiation of Bloch simulations. *Magn Reson Med.* 2019;82(4):1438-1451.
22. van der Heide O, Sbrizzi A, Luijten PR, van den Berg CAT. High-resolution in vivo MR-STAT using a matrix-free and parallelized reconstruction algorithm. *NMR Biomed.* 2020;33(4):e4251.
23. da Cruz G, Bustin A, Jaubert O, Schneider T, Botnar RM, Prieto C. Sparsity and locally low rank regularization for MR fingerprinting. *Magn Reson Med.* 2019;81(6):3530-3543.
24. Emmerich J, Flassbeck S, Schmidt S, Bachert P, Ladd ME, Straub S. Rapid and accurate dictionary-based T2 mapping from multi-echo turbo spin echo data at 7 Tesla. *J Magn Reson Imaging.* 2019;49(5):1253-1262.
25. Hilbert T, Xia D, Block KT, et al. Magnetization transfer in magnetic resonance fingerprinting. *Magn Reson Med.* 2020;84(1):128-141.
26. Sobol WT, Gauntt DM. On the stationary states in gradient echo imaging. *J Magn Reson Imaging.* 1996;6(2):384-398.
27. Ma D, Coppo S, Chen Y, et al. Slice profile and B1 corrections in 2D magnetic resonance fingerprinting. *Magn Reson Med.* 2017;78(5):1781-1789.
28. Ben-Eliezer N, Sodickson DK, Block KT. Rapid and accurate T2 mapping from multi-spin-echo data using Bloch-simulation-based reconstruction. *Magn Reson Med.* 2015;73(2):809-817.
29. Niu MY, Horesh L, Chuang I. Recurrent neural networks in the eye of differential equations. *arXiv Prepr arXiv190412933*; 2019.
30. Sundermeyer M, Schlüter R, Ney H. LSTM neural networks for language modeling. In: Thirteenth Annual Conference of the International Speech Communication Association; 2012.
31. Cho K, Van Merriënboer B, Gulcehre C, et al. Learning phrase representations using RNN encoder-decoder for statistical machine translation. *arXiv Prepr arXiv14061078*; 2014.
32. Pauly J, Nishimura D, Macovski A. A k-space analysis of small-tip-angle excitation. *J Magn Reson.* 1989;81(1):43-56.
33. Buonincontri G, Sawiak SJ. MR fingerprinting with simultaneous B1 estimation. *Magn Reson Med.* 2016;76(4):1127-1135.
34. van Valenberg W. Radiofrequency pulse design through optimal control and model order reduction of the Bloch equation. Master Thesis. Faculty of Science Theses, Utrecht University Repository; 2015.
35. Glowinski R, Osher SJ, Yin W. *Splitting Methods in Communication, Imaging, Science, and Engineering*. Springer; 2017.
36. Guenthner C, Kozerke S. Unifying Extended Phase Graphs and k-space Readout. In: *Proceedings of the 27th Annual Meeting of ISMRM, Montreal*; 2019.
37. Malik SJ, Sbrizzi A, Hoogduin H, Hajnal J V. Equivalence of EPG and isochromat-based simulation of MR signals. In: *Proceedings of the 24th Annual Meeting of ISMRM, Singapore*; 2016:3196.
38. Hermans M, Schrauwen B. Training and analysing deep recurrent neural networks. *Adv Neural Inf Process Syst.* 2013;26:190-198.
39. In den Kleef JJ, Cuppen JJ. RLSQ: T1, T2, and rho calculations, combining ratios and least squares. *Magn Reson Med.* 1987;5(6):513-524.
40. Abadi M, Agarwal A, Barham P, et al. Tensorflow: Large-scale machine learning on heterogeneous distributed systems. *arXiv Prepr arXiv160304467*; 2016.
41. Kingma DP, Ba J. Adam: A method for stochastic optimization. *arXiv Prepr arXiv14126980*; 2014.

42. Winkelmann S, Schaeffter T, Koehler T, Eggers H, Doessel O. An optimal radial profile order based on the Golden Ratio for time-resolved MRI. *IEEE Trans Med Imaging.* 2006;26(1):68-76.
43. Aubert-Broche B, Evans AC, Collins L. A new improved version of the realistic digital brain phantom. *Neuroimage.* 2006;32(1):138-145.
44. Assländer J, Cloos MA, Knoll F, Sodickson DK, Hennig J, Lattanzi R. Low rank alternating direction method of multipliers reconstruction for MR fingerprinting. *Magn Reson Med.* 2018;79(1):83-96.
45. Cowan G. *Statistical Data Analysis*. Oxford, UK: Oxford University Press; 1998.
46. van Riel MHC, Yu Z, Hodono S, et al. Optimization of MR Fingerprinting for Free-Breathing Quantitative Abdominal Imaging. *arXiv Prepr arXiv200602928*; 2020.
47. Nocedal J, Wright S. *Numerical Optimization*. Berlin/Heidelberg, Germany: Springer Science & Business Media; 2006.
48. Storn R, Price K. Differential evolution-a simple and efficient heuristic for global optimization over continuous spaces. *J Glob Optim.* 1997;11(4):341-359.
49. Lampinen J. A constraint handling approach for the differential evolution algorithm. In: *Proceedings of the 2002 Congress on Evolutionary Computation*. CEC'02 (Cat. No. 02TH8600), Vol. 2; 2002:1468-1473.
50. Virtanen P, Gommers R, Oliphant TE, et al. SciPy 1.0: fundamental algorithms for scientific computing in Python. *Nat Methods.* 2020;17(3):261-272.
51. Ostenson J, Smith DS, Does MD, Damon BM. Slice-selective extended phase graphs in gradient-crushed, transient-state free precession sequences: An application to MR fingerprinting. *Magn Reson Med.* 2020;84(6):3409-3422.
52. Malik SJ, Teixeira RPAG, Hajnal JV. Extended phase graph formalism for systems with magnetization transfer and exchange. *Magn Reson Med.* 2018:80(2):767-779.
53. Tan C, Sun F, Kong T, Zhang W, Yang C, Liu C. A survey on deep transfer learning. In: *International Conference on Artificial Neural Networks*; 2018:270-279.
54. Holmes C, Mawhirter D, He Y, Yan F, Wu B. Grnn: Low-latency and scalable rnn inference on gpus. In: *Proceedings of the Fourteenth EuroSys Conference*; 2019:1-16.

SUPPORTING INFORMATION

Additional supporting information may be found online in the Supporting Information section at the end of this article.

How to cite this article: Liu H, van der Heide O, van den Berg CAT, Sbrizzi A. Fast and accurate modeling of transient-state, gradient-spoiled sequences by recurrent neural networks. *NMR in Biomedicine*. 2021;34:e4527. https://doi.org/10.1002/nbm.4527